PHILOSOPHICAL TRANSACTIONS A

royalsocietypublishing.org/journal/rsta

Research

Cite this article: Sigurðardóttir A, Barnard J, Bullamore D, McCormick A, Cartwright J, Cardoso S. 2020 Radial spreading of turbulent bubble plumes. *Phil. Trans. R. Soc. A* **378**: 20190513.
http://dx.doi.org/10.1098/rsta.2019.0513

Accepted: 11 May 2020

One contribution of 13 to a theme issue 'Stokes at 200 (part 2)'.

Subject Areas:
fluid mechanics

Keywords:
plume, bubbles, mixing

Authors for correspondence:
Arna Sigurðardóttir
e-mail: as2817@cam.ac.uk
Jonathan Barnard
e-mail: jmb268@cam.ac.uk
Julyan Cartwright
e-mail: julyan.cartwright@csic.es
Silvana Cardoso
e-mail: sssc1@cam.ac.uk

Radial spreading of turbulent bubble plumes

Arna Sigurðardóttir[1], Jonathan Barnard[1], Danielle Bullamore[1], Amy McCormick[1], Julyan Cartwright[2,3] and Silvana Cardoso[1]

[1]Department of Chemical Engineering and Biotechnology, University of Cambridge, Cambridge, UK
[2]Instituto Andaluz de Ciencias de la Tierra, CSIC–Universidad de Granada, 18100 Armilla, Granada, Spain
[3]Instituto Carlos I de Física Teórica y Computacional, Universidad de Granada, 18071 Granada, Spain

JC, 0000-0001-7392-0957; SC, 0000-0003-0417-035X

Weak bubble plumes carry liquid from the environment upwards and release it at multiple intermediate levels in the form of radial intrusive currents. In this study, laboratory experiments are performed to explore the spreading of turbulent axisymmetric bubble plumes in a liquid with linear density stratification. The thickness, volumetric flowrate and spreading rates of multiple radial intrusions of plume fluid were measured by tracking the movement of dye injected at the source of bubbles. The experimental results are compared with scaling predictions. Our findings suggest that the presence of multiple intrusions reduces their spreading rate, compared to that of a single intrusion. This work is of relevance to the spreading of methane plumes issuing from the seabed in the Arctic Ocean, above methane-hydrate deposits. The slower, multiple spreading favours the presence of methane-rich seawater close to the plume, which may reduce the dissolution of methane in the bubbles, and thus promote the direct transport of methane to the atmosphere.

This article is part of the theme issue 'Stokes at 200 (part 2)'.

1. Introduction

In 1851, Stokes derived an expression for the drag on a spherical pendulum bob moving in a viscous fluid [1]. This expression, by a modification of the

THE ROYAL SOCIETY PUBLISHING

boundary conditions, can describe the drag on a spherical bubble, and a further reshaping can also approximate the drag on a non-spherical bubble. Many such bubbles together constitute either a bubble cloud or a bubble plume. Bubble plumes are formed above a continuous source of gas bubbles in a liquid environment. The bubbles rise owing to buoyancy and carry ambient fluid upwards forming a plume of two phases [2–5]. The bubbles originate either from point sources that form axisymmetric plumes, or line sources that give rise to two-dimensional plumes. In weak bubble plumes, a double structure develops: the bubbles are concentrated in a central region, around which liquid rises [6–8]. The outer liquid plume rises more slowly than the inner plume and entrains ambient liquid. Liquid between the inner and outer plumes is exchanged by turbulent eddies. In a linear density stratification, the bubbles carry the negatively buoyant liquid upwards over only a relatively short distance, subsequently releasing it to the environment. This liquid from the outer plume then descends to a level of neutral buoyancy where it spreads horizontally. The liquid peeling occurs periodically throughout the vertical extent of the plume. The horizontal plume-liquid currents spreading in the environment are called intrusions. Similar mechanisms of intrusion formation have been described for gravity currents [9] and single-phase plumes [10] in stratified environments.

Intrusive gravity currents, formed from direct injection of fluid or by a single-phase plume in a stratified environment, have been of interest to many researchers [11–15]. Intrusion behaviour is characterized in terms of two spreading regimes when buoyancy is driving the flow. The initial spreading is determined by a balance of the inertial retarding force and the buoyancy force, leading to the spreading relation [16]

$$R = a(NQ_i)^{1/3}t^{2/3}, \tag{1.1}$$

where R is the radial position of the tip of the intrusion, N is the ambient buoyancy frequency, Q_i is the intrusion volumetric flowrate, and t is time. This balance corresponds to an intrusion Froude number $Fr = 8\pi a^3/9$ [17,18]. At later times, the intrusion flow is slower, so that viscous forces become important. Once the viscous-buoyancy regime is established, the tip of the intrusion moves according to [16]

$$R = b\left(\frac{N^2Q_i^4}{\nu}\right)^{1/10}t^{1/2}, \tag{1.2}$$

where ν is the kinematic viscosity. Lemckert & Imberger [16] proposed a time-scale for the change of regime, from the time taken for the inertia-buoyancy current thickness to collapse to the viscous-buoyancy one, as

$$t_r \sim N^{-1}G = N^{-1}\left(\frac{Q_i^2N}{\nu^3}\right)^{1/5}. \tag{1.3}$$

Previous experimental and theoretical work suggests the ranges $a = 0.40 - 0.80$ and $b = 0.45 - 0.52$ [11–13,16,19].

The initial vertical thickness of the intrusion formed from plume spreading is generally agreed to follow the scaling

$$L = cB_0^{1/4}N^{-3/4}, \tag{1.4}$$

where B_0 is the buoyancy flux at the source of the plume [5,20]. The exact value of the coefficient depends on the relative speeds of the bubbles and the plume. The typical range is $c \sim 0.7$–4.5, the higher values being observed for higher plume speeds [5,20].

In contrast to the above work on single intrusions, weak bubble plumes spread forming multiple intrusions, between which ambient fluid is entrained into the plume. This periodic spreading pattern has not been studied quantitatively before. In this work, laboratory experiments are performed to explore the spreading of weak axisymmetric bubble plumes in a liquid with linear density stratification. The thickness, volumetric flowrate and spreading rates of the multiple radial intrusions were measured by tracking the movement of dye injected at the source of bubbles. This preliminary study helps the understanding of the structure and spreading

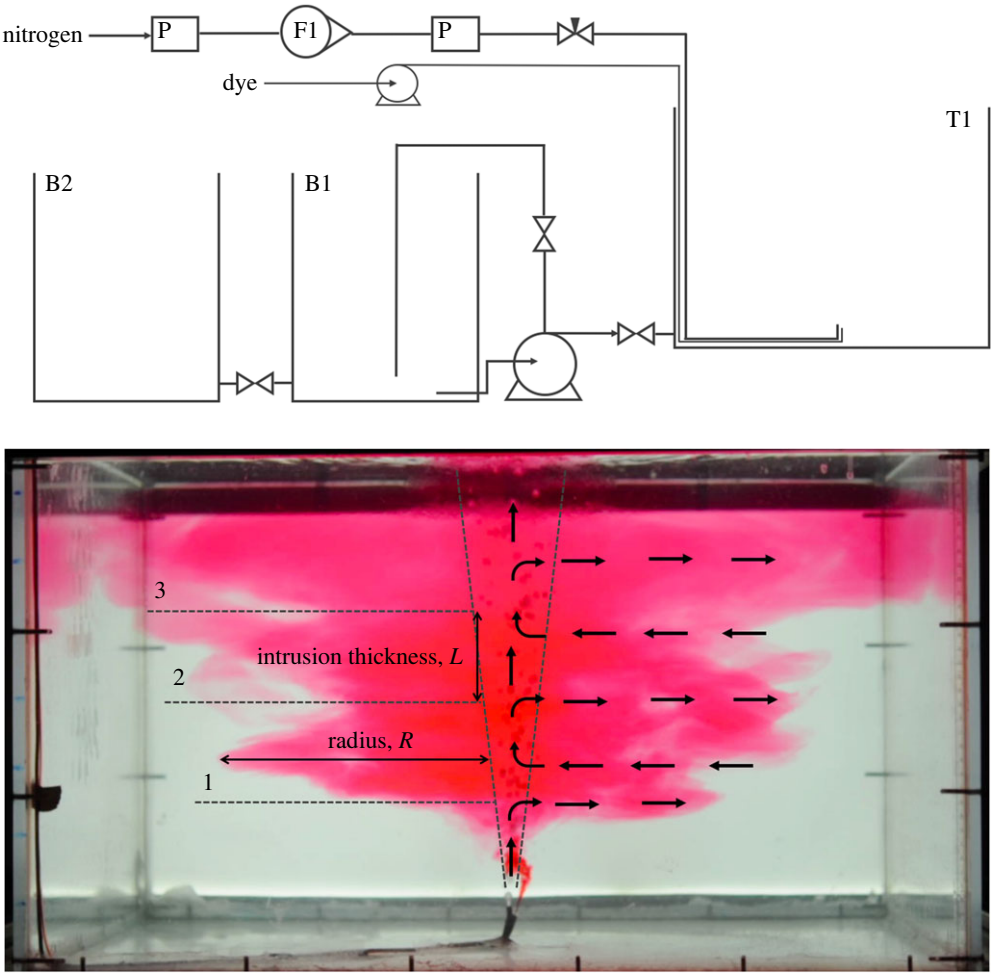

Figure 1. (*a*) Schematic of the experimental set-up. (*b*) General pattern of plume spreading. For each intrusion, the radius R; the volumetric flow rate Q_i; and the intrusion thickness at the edge of the plume L, were measured. The edge of the plume is taken to be the radius of the bubble core, indicated by the dotted lines. Black arrows illustrate the flow of liquid. Intrusions are numbered from the bottom as shown. (Online version in colour.)

of methane bubble plumes in the Arctic sea. Numerous such plumes transport the methane from depth to shallower regions in the seawater, and possibly to the atmosphere [21–23].

2. Experimental procedure

Laboratory experiments were carried out using the equipment shown schematically in figure 1*a*.

Tank T1 was made of perspex and had inner dimensions of 68 × 68 × 50 cm. A double bucket system (B1 and B2) was used to create a linear density profile [24]. The density profile in tank T1 was measured using an Anton Paar density metre. Nitrogen gas was supplied into tank T1 at height 2.5 cm above the tank base using a stainless steel tube with a diameter of 1 mm (with the exception of three experiments where a 0.5 mm tube was used, marked with asterisks (*) in table 1), forming a stream of bubbles. The flowrate of nitrogen was measured with a rotameter and controlled with a needle valve. Pressure in the nitrogen supply line was kept constant at 2 bar. The bubbles formed were ellipsoidal, with diameters in the range 0.2–1.2 cm. The bubble size can be assumed constant owing to negligible breakup, coalescence and expansion over the small height of the tank [25]. Dye was fed into the tank at the same height as the gas using a syringe pump via

Table 1. Experiments conducted.

experiment	Q_0 (cm^3 s^{-1})	N (s^{-1})	intrusions	U_N
1*	20	1.10	2	2.00
2*	20	1.45	3	1.87
3	18	0.79	1	2.25
4	18	1.03	2	2.10
5	18	1.12	2	2.06
6	18	1.25	2	2.00
7	15	0.82	2	2.32
8	15	0.93	2	2.25
9	15	1.22	2	2.10
10*	15	1.35	3	2.05
11	10	0.97	3	2.46
12	10	1.02	3	2.43
13	10	1.11	3	2.38
14a	10	1.23	4	2.31
14b	10	1.23	4	2.31
15	10	1.45	4	2.23
16	5	1.04	3	2.88
17a	5	0.92	3	2.97
17b	5	0.92	3	2.97
17c	5	0.92	3	2.97
17d	5	0.92	3	2.97
17e	5	0.92	3	2.97
17f	5	0.92	3	2.97

a silicone tube of diameter 1 mm. The dye was a 5 g l^{-1} mixture of Acid Red 1 (Azophloxine) in water and delivered at a rate of 5 cm^3 min^{-1}.

A Nikon D300s DSLR camera with an AF-S Micro NIKKOR 60 mm f/2.8G ED lens was used to capture the experiments at 24 Hz and the images were processed using the MATLAB R2017b image processing toolbox. To ensure consistent lighting of the videos for image processing, an LED light sheet was placed behind the tank and all other light was eliminated by turning off ceiling lights and using two sets of blinds on the windows. From tracking the movement of the dye, the radius and thickness of each intrusion, as well as the total volume within it could be determined (figure 1*b*). Further details of the image processing are given in [26–28].

The experiments conducted in this project are given in table 1 (complete raw data may be found at https://doi.org/10.17863/CAM.51658). The slip velocity of the bubbles u_s is presented in non-dimensional form $U_N = u_s/(B_0 N)^{1/4}$. For most of the range of U_N studied, the bubble plumes have distinct and steady sub-surface intrusions [5,7].

3. Results and discussion

Figure 2 shows the typical evolution of the spreading of the bubble plumes. The injected red dye is quickly diluted within the plume and carried upwards. At early times, multiple intrusions

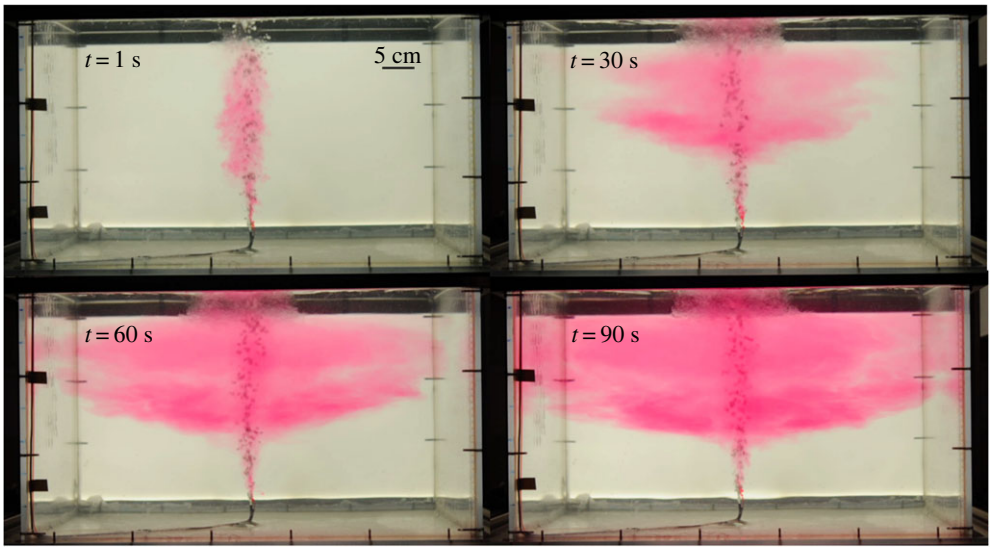

Figure 2. Spreading of a bubble plume with gas flowrate 17.7 $cm^3\ s^{-1}$, in stratification with $N = 1.25\ s^{-1}$ (experiment 6). (Online version in colour.)

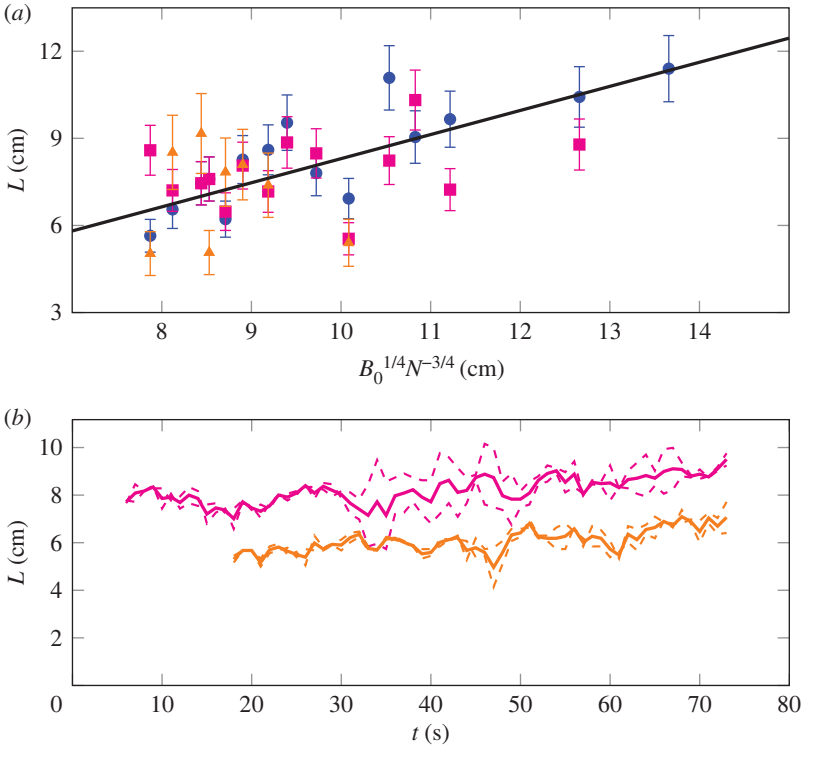

Figure 3. (*a*) Instantaneous intrusion thickness against the Ozmidov length, where the points correspond to intrusion numbers 1, yellow triangles; 2, pink squares; 3, blue circles counted from below. The scaling is constrained to intersect the origin. The errorbars represent the standard deviation of results from repeated experiments. (*b*) Evolution of the thickness of intrusions 1, bottom yellow; 2, top pink solid lines for experiment 17b. Dashed lines show variations between results from the left and right side of the plume images. (Online version in colour.)

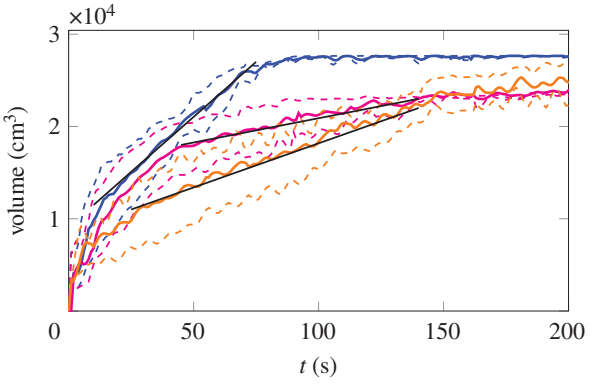

Figure 4. Intrusion volume with respect to time for Experiment 17f. Coloured lines correspond to the volume of intrusion 1, bottom yellow; 2, intermediate pink; 3, top blue, solid lines. Coloured dashed lines show variations between results from the left and right side of the plume images. The slope of the best line through the data is the volumetric flowrate of the intrusion, Q_i. (Online version in colour.)

develop, which gradually spread radially. The entrainment of ambient fluid into the plume occurs in the non-dyed fluid region below and between the intrusions. Once the intrusions reach the wall of the tank, the dyed fluid is re-entrained into the plume and eventually fills the entire tank.

The intrusion thickness, measured at the edge of the plume, is approximately independent of time and proportional to the Ozmidov length [5], as shown in figure 3. The results are separated by intrusion number and can be seen to follow the expected scaling (1.4) with a coefficient $c = 0.83 \pm 0.14$. The measurements presented are instantaneous ones; the typical time evolution is shown in figure 3*b* for intrusions 1 and 2 in experiment 17d. The scatter of the data in the time evolution is consistent with that in the scaling. The difficulty in measuring the intrusion thickness using image processing, owing to the local mixing produced by the bubble core, precluded the use of a time-averaged thickness for all intrusions.

The intrusion flowrates, Q_i, were determined from the slope of the straight line fit for the intrusion volume as a function of time (figure 4). The intrusion volume was calculated by measuring the intrusion thickness as a function of radius at each time, from the two-dimensional image view from the front of the tank, and integrating assuming axisymmetry. However, discrepancies were observed to occur between the right and left sides of each current, as seen in figure 4, partly owing to the axisymmetric assumption. The initial behaviour, while the plume is established, was neglected in the calculation of the flowrate. The large-time behaviour with an apparent constant volume is an image-processing artefact, and was also neglected. Indeed, as an intrusion approaches the tank wall, it spreads vertically; this spreading was neglected in the calculation of the intrusion volume flux owing to the utilization of an image-analysis control volume of set height. The set control volume height results in the flattening of the volume curves, as shown in figure 4, and allows the intrusion volume flux to be determined from the curve using the largest time interval with an approximately constant slope prior to any intrusion interaction with the wall.

Figure 5 shows the intrusion flowrate plotted against the scaling group $B_0^{3/4}N^{-5/4}$. The flowrate is larger for the top intrusion owing to the release of the liquid carried with the bubbles in the central part of the plume, in addition to the liquid dragged in the outer plume. For the lower intrusions, 1 and 2, the flowrate follows the expected scaling (1.4) with a coefficient 0.13 ± 0.06. This flux is much lower than that reported by Socolofsky *et al.* [7] for sediment plumes in the same range of U_N (their fig. 8), possibly owing to the much weaker plumes studied here. The relatively large experimental error is a result of the deviation of the plume spreading from the exact axisymmetric one and is consistent with the magnitude of the difference between the left- and right-hand side results presented in figure 4.

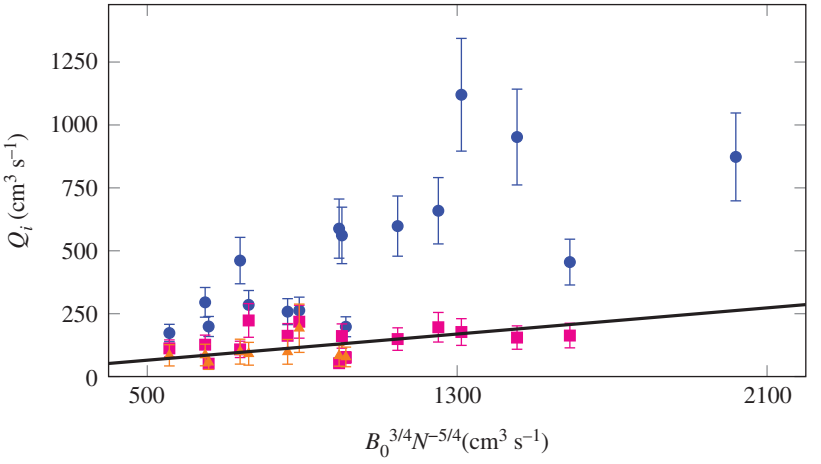

Figure 5. Intrusion flowrate against $B_0^{3/4}N^{-5/4}$. Points correspond to intrusion numbers: 1, yellow triangles; 2, pink squares; 3, blue circles. The scaling is constrained to intersect the origin. The errorbars represent the standard deviations of results from repeated experiments. (Online version in colour.)

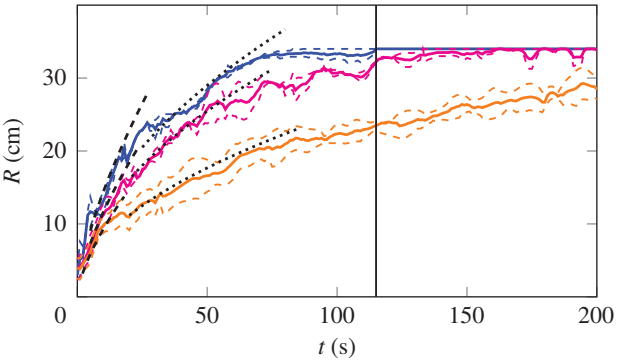

Figure 6. Intrusion radius with respect to time for experiment 17b. Solid lines correspond to average radius for intrusion 1, bottom yellow; 2, intermediate pink; 3, top blue lines. Coloured dashed lines show variations between results from the left and right side of the plume images. Predicted inertia-buoyancy ($R \propto t^{2/3}$) and viscous-buoyancy ($R \propto t^{1/2}$) regimes are shown by black dashed lines and black dotted lines, respectively. The vertical line signals the time at which the first intrusion reaches the wall of the tank. (Online version in colour.)

Figure 6 presents the radial spreading of several intrusions as a function of time. The inertia-buoyancy and viscous-buoyancy regimes were identified, from the changing slopes, from $t^{2/3}$ in the inertia-buoyancy regime to $t^{1/2}$ in the viscous-buoyancy regime, as shown. In the experiments presented here, the transition time between the inertia-buoyancy and viscous-buoyancy regimes from (1.3) is expected to be about 100 s. The results indicate on average a lower transition time of around 20 s, which may be explained by the counterflow present in the multiple intrusions studied here. In each experiment, the top intrusion reached the wall of the tank after approximately 100 s.

The results from all the experiments are presented in figures 7 and 8 for the inertia-buoyancy and viscous-buoyancy regimes, respectively. The reference time, t_r, and reference radius, R_r, are taken to be the time and radius at which the transition to the viscous regime occurs. In the inertia-buoyancy regime, the plume radius, b_p, is used as a reference.

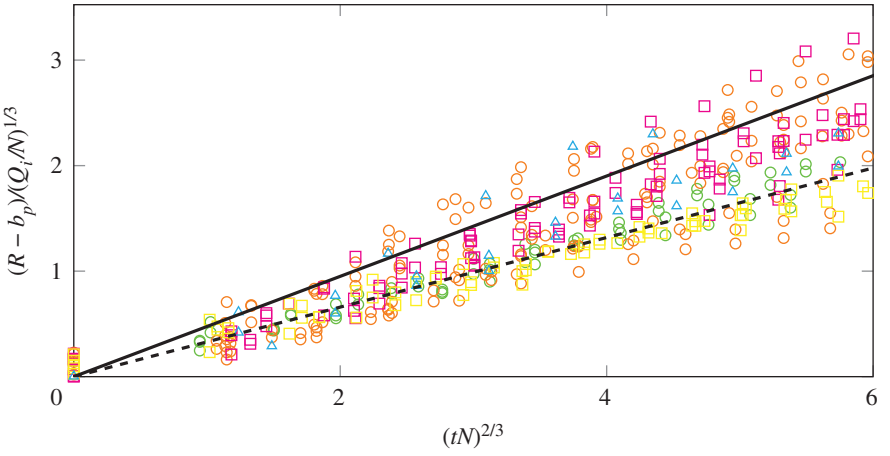

Figure 7. Dimensionless intrusion radius with respect to dimensionless time in the inertia-buoyancy regime. Points correspond to bubble flowrates of $Q_0 = 5$ cm^3 s^{-1} (green circles); 10 cm^3 s^{-1} (red circles); 15 cm^3 s^{-1} (pink squares); 18 cm^3 s^{-1} (yellow squares) and 20 cm^3 s^{-1} (blue triangles). The black line and dashed line represent a Froude number of 0.3 and 0.1 respectively. (Online version in colour.)

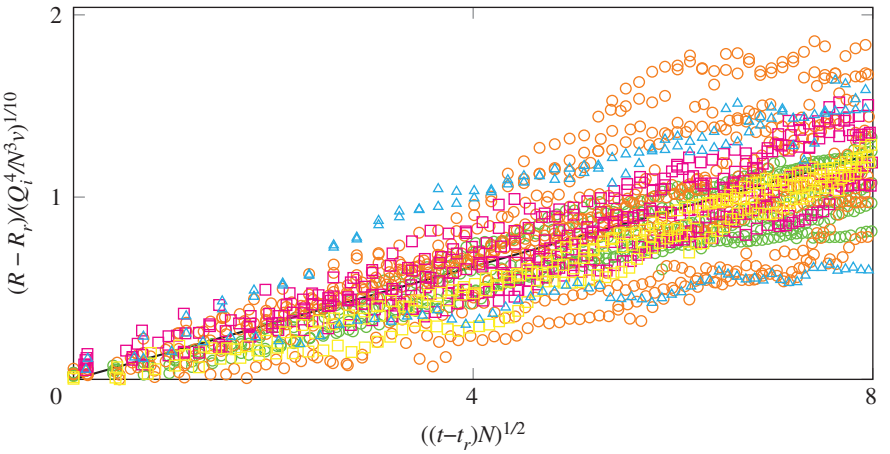

Figure 8. Dimensionless intrusion radius with respect to dimensionless time in the viscous-buoyancy regime. Points correspond to bubble flowrates of $Q_0 = 5$ cm^3 s^{-1} (green circles); 10 cm^3 s^{-1} (red circles); 15 cm^3 s^{-1} (pink squares); 18 cm^3 s^{-1} (yellow squares) and 20 cm^3 s^{-1} (blue triangles). The black line represents the average scaling. (Online version in colour.)

The spreading relationship determined for the inertia-buoyancy regime is $R = 0.39(NQ_i)^{1/3}t^{2/3}$, corresponding to an average Froude number of $Fr = 0.17$. The coefficient has a standard deviation of 0.08, corresponding to a Froude-number range of $0.09 < Fr < 0.31$. For the viscous-buoyancy regime, we obtained $R = 0.15(N^2Q_i^4/\nu)^{1/10}t^{1/2}$, where the coefficient has a standard deviation of 0.02. The presence of the tank wall slows the spreading rate of the intrusion at large times in this regime, as noted in previous work [12]. The intrusion radius beyond which the presence of the wall became important varied for each experiment. To prevent wall effects from influencing the calculation of the intrusion spreading rate, we neglected all radial measurements beyond which there was an obvious gradient reduction without subsequent recovery back to the original gradient. The offsets b_p, R_r and t_r used in figures 7 and 8 are presented in figure 9 as a function of the experimental parameters. The offset of 0.20 from the origin in figure 9*a* is associated with the plume originating from a real source. Assuming a plume spread similar to that of a single-phase

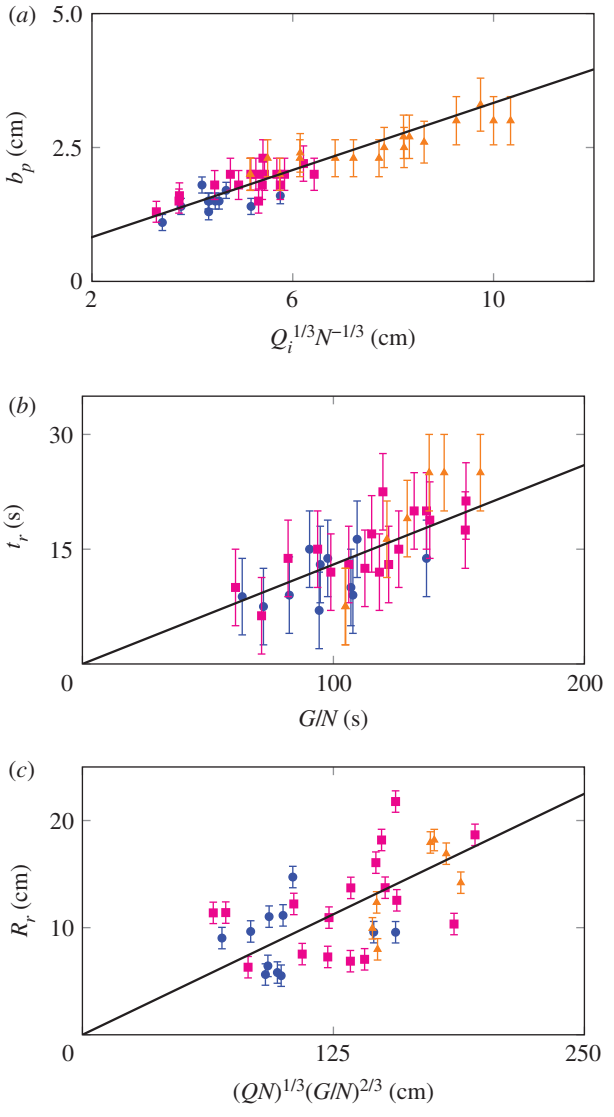

Figure 9. The points correspond to intrusion numbers 1, blue circles; 2, pink squares; 3, yellow triangles counted from below. (*a*) Plume radius b_p against the Ozmidov length. The line of best fit has a coefficient of 0.33 ± 0.07. (*b*) Reference time t_r against G/N as predicted by the scaling (1.3). The line of best fit has a coefficient of 0.13 ± 0.05. (*c*) Reference radius R_r against the length scale predicted by (1.3) and (1.1). The line of best fit has a coefficient of 0.09 ± 0.03. (Online version in colour.)

plume in an unstratified environment, the average virtual source is 2.6 cm below the real source for an average plume entrainment coefficient $\alpha = 0.063$, aligning with previous measurements for weak bubble plumes [2]. The scatter in figure 9*c* reflects the difficulty in setting the transition between the inertia and viscous regimes and partly explains the spread of data in figure 8.

Table 2 compares these results to previous work in linear density stratification, with either direct injection of fluid into an intrusion or a plume intrusion. Although we do not present the results of Kotsovinos [14] for a jet intrusion, owing to the different scaling used in that study, it is worth noting that his results (see his figs 14 and 15) are in quantitative agreement with those of Zatsepin & Shapiro [13] and Lemckert & Imberger [16]. For the inertia-buoyancy regime, our finding of 0.39 is consistent with the measurement of Lemckert & Imberger [16] for a single intrusion formed from a bubble plume. The theoretical result of Chen [11] is much larger, of 0.802.

Table 2. Comparison of coefficients for the inertia-buoyancy and viscous-buoyancy regimes for radial intrusions in linear stratification.

study	inertia-buoyancy coefficient, a	viscous-buoyancy coefficient, b	type of flow
Chen [11]	0.802	0.45	asymptotic solutions for submerged spreading.
Zatsepin & Shapiro [13]	not studied	0.52	laboratory experiments: Constant discharge at level of neutral buoyancy.
Ivey & Blake [12]	not studied	0.45	laboratory experiments: Constant discharge at level of neutral buoyancy.
Lemckert & Imberger [16]	0.40 ± 0.13	not studied	field experiments: Intrusions generated by deep-set point-source bubble plume systems.
current results	0.39 ± 0.08	0.15 ± 0.02	laboratory experiments: Intrusions of point-source bubble-plumes.

The speed of the intrusion in this regime is largely set by the energy dissipation at its nose [15], so the consistency of the coefficients for single and multiple spreadings suggests that the periodic counterflow of environment fluid in the latter does not affect the energy balance. For the viscous-buoyancy regime, the theoretical results of Chen [11], and the experimental results of Ivey & Blake [12] and Zatsepin & Shapiro [13], for direct injection of fluid, are in the narrow range of 0.45–0.52. The coefficient found in our work for multiple bubble-plume intrusions is significantly smaller. The slower spreading in our study may be explained by the counter flow of the environmental fluid between the multiple intrusions, as it is entrained into the plume. Although this counter flow does not seem to affect the dissipation of energy at the nose of the intrusion in the inertia-buoyancy regime, a higher viscous friction is expected at lower speeds. Our findings suggest that dissolved methane may be retained relatively close to rising methane bubble plumes in the Arctic sea, thus reducing the dissolution of methane and promoting the direct transport of methane to the atmosphere.

4. Conclusion

Laboratory experiments were performed to quantify the spreading of turbulent axisymmetric bubble plumes in a linear-density stratification. Weak bubble plumes characterized by multiple, periodic radial intrusions were considered. It was found that the spreading in the inertia-buoyancy regime was slower than theoretical results for single intrusions but consistent with experimental observations of bubble plume systems forming single intrusions. This consistency of the intrusion speed for single and multiple spreadings suggests that the periodic counterflow of environment fluid in the latter does not affect the energy balance at the nose of an intrusion. Spreading in the viscous-buoyancy regime was significantly slower than that reported from both theoretical and experimental results for single intrusions formed by direct injection of fluid. This slower spreading may be explained by the higher viscous friction caused by the counter flow of the environmental fluid between multiple intrusions, as it is entrained into the plume. This finding is of relevance to the spreading of dissolved methane by bubble plumes in the Arctic Sea.

Data accessibility. All data are included in the paper and at repository https://doi.org/10.17863/CAM.51658.

Authors' contributions. All authors contributed to the paper.
Competing interests. We declare we have no competing interests.
Funding. J.M.B. acknowledges financial support from the Woolf Fisher Trust for his PhD study. J.H.E.C. acknowledges the financial support of the Spanish MINCINN project FIS2016-77692-C2-2-P. S.S.S.C. acknowledges the financial support of the UK Leverhulme Trust project RPG-2015-002.

References

1. Stokes GG. 1851 On the effect of internal friction of fluids on the motion of pendulums. *Trans. Camb. Philos. Soc.* **9**, 8–106.
2. Milgram JH. 1983 Mean flow in round bubble plumes. *J. Fluid Mech.* **133**, 345–376. (doi:10.1017/S0022112083001950)
3. Schladow SG. 1992 Bubble plume dynamics in a stratified medium and the implications for water quality amelioration in lakes. *Water Resour. Res.* **28**, 313–321. (doi:10.1029/91WR02499)
4. Wüest A, Brooks NH, Imboden DM. 1992 Bubble plume modeling for lake restoration. *Water Resour. Res.* **28**, 3235–3250. (doi:10.1029/92WR01681)
5. Asaeda T, Imberger J. 1993 Structure of bubble plumes in linearly stratified environments. *J. Fluid Mech.* **249**, 35–57. (doi:10.1017/S0022112093001065)
6. McDougall TJ. 1978 Bubble plumes in stratified environments. *J. Fluid Mech.* **85**, 655–672. (doi:10.1017/S0022112078000841)
7. Socolofsky SA, Adams EE. 2003 Liquid volume fluxes in stratified multiphase plumes. *J. Hydraul. Eng. ASCE* **129**, 905–914. (doi:10.1061/(ASCE)0733-9429(2003)129:11(905))
8. Socolofsky SA, Adams EE. 2005 Role of slip velocity in the behavior of stratified multiphase plumes. *J. Hydraul. Eng. ASCE* **131**, 273–282. (doi:10.1061/(ASCE)0733-9429(2005)131:4(273))
9. Hogg C, Dalziel S, Huppert H, Imberger J. 2017 Inclined gravity currents filling basins: the impact of peeling detrainment on transport and vertical structure. *J. Fluid Mech.* **820**, 400–423. (doi:10.1017/jfm.2017.196)
10. Gladstone C, Woods AW. 2014 Detrainment from a turbulent plume produced by a vertical line source of buoyancy in a confined, ventilated space. *J. Fluid Mech.* **742**, 35–49. (doi:10.1017/jfm.2013.640)
11. Chen JC. 1980 Studies on gravitational spreading currents. PhD thesis, Caltech, Pasadena, CA, USA.
12. Ivey GN, Blake S. 1985 Axisymrnetric withdrawal and inflow in a density-stratified container. *J. Fluid Mech.* **161**, 115–137. (doi:10.1017/S0022112085002841)
13. Zatsepin AG, Shapiro GI. 1982 A study of axisymmetric intrusions in a stratified fluid. *Izv. Atmos. Oceanic Phys.* **18**, 77–80.
14. Kotsovinos NE. 2000 Axisymmetric submerged intrusion in stratified fluid. *J. Hydraul. Eng. ASCE* **126**, 446–456. (doi:10.1061/(ASCE)0733-9429(2000)126:6(446))
15. Ungarish M. 2009 *An introduction to gravity currents and intrusions*. New York, NY: Chapman and Hall/CRC.
16. Lemckert CJ, Imberger J. 1993 Axisymmetric intrusive gravity currents in linearly stratified fluids. *J. Hydraul. Eng. ASCE* **119**, 662–679. (doi:10.1061/(ASCE)0733-9429(1993)119:6(662))
17. Woods AW. 2010 Turbulent plumes in nature. *Annu. Rev. Fluid Mech.* **42**, 391–412. (doi:10.1146/annurev-fluid-121108-145430)
18. Rooney GG, Devenish BJ. 2014 Plume rise and spread in a linearly stratified environment. *Geophys. Astrophys. Fluid Dyn.* **108**, 168–190. (doi:10.1080/03091929.2013.849345)
19. Maxworthy T, Leilich J, Simpson JE, Meiburg EH. 2002 The propagation of a gravity current into a linearly stratified fluid. *J. Fluid Mech.* **453**, 371–394. (doi:10.1017/S0022112001007054)
20. Chen MH. 2001 Bubble plumes. PhD thesis, Department of Chemical Engineering, University of Cambridge, UK.
21. Shakhova N, Semiletov I, Chuvilin E. 2019 Understanding the permafrost-hydrate system and associated methane releases in the east Siberian arctic shelf. *Geosciences* **9**, 251. (doi:10.3390/geosciences9060251)
22. Shakhova N, Semiletov I, Salyuk A, Yusupov V, Kosmach D, Gustafsson Ö. 2010 Extensive methane venting to the atmosphere from sediments of the east siberian arctic shelf. *Science* **327**, 1246–1250. (doi:10.1126/science.1182221)

23. Shakhova N *et al*. 2015 The east Siberian arctic shelf: towards further assessment of permafrost-related methane fluxes and role of sea ice. *Phil. Trans. R. Soc. A* **373**, 20140451. (doi:10.1098/rsta.2014.0451)
24. Oster G, Yamamoto M. 1963 Density gradient techniques. *Chem. Rev.* **63**, 257–268. (doi:10.1021/cr60223a003)
25. Clift R, Grace JR, Weber ME. 1978 *Bubbles, drops, and particles*. Mineola, NY: Dover Publications.
26. Bullamore D. 2019 Methane plumes in the Arctic. CET IIB thesis, Department of Chemical Engineering and Biotechnology, University of Cambridge, UK.
27. McCormick A. 2019 Methane bubble plumes in the Arctic. CET IIB thesis, Department of Chemical Engineering and Biotechnology, University of Cambridge, UK.
28. Sigurðardóttir A. 2019 Mixing induced by bubble plumes. MPhil thesis, Department of Chemical Engineering and Biotechnology, University of Cambridge, UK.